

Article

Low-Profile Broadband Dual-Polarized Dipole Antenna for Base Station Applications

Hao Feng ¹, Mengyuan Li ², Zhiyi Zhang ^{3,*}, Jiahui Fu ¹, Qunhao Zhang ¹ and Yulin Zhao ⁴¹ School of Electronics and Information Engineering, Harbin Institute of Technology, Harbin 150001, China² AVIC Research Institute for Special Structures of Aeronautical Composites, Jinan 250104, China³ Department of Electrical Engineering, City University of Hong Kong, Hong Kong SAR, China⁴ College of Metrology and Measurement Engineering, China Jiliang University, Hangzhou 314423, China

* Correspondence: zhiyi.zhang@my.cityu.edu.hk

Abstract: A low-profile broadband dual-polarized antenna is investigated for base station applications. It consists of two orthogonal dipoles, fork-shaped feeding lines, an artificial magnetic conductor (AMC), and parasitic strips. By utilizing the Brillouin dispersion diagram, the AMC is designed as the antenna reflector. It has a wide in-phase reflection bandwidth of 54.7% (1.54–2.70 GHz) and a surface-wave bound range of 0–2.65 GHz. This design effectively reduces the antenna profile by over 50% compared to traditional antennas without an AMC. For demonstration, a prototype is fabricated for 2G/3G/LTE base station applications. Good agreement between the simulations and measurements is observed. The measured -10 -dB impedance bandwidth of our antenna is 55.4% (1.58–2.79 GHz), with a stable gain of 9.5 dBi and a high isolation of more than 30 dB across the impedance passband. As a result, this antenna is an excellent candidate for miniaturized base station antenna applications.

Keywords: dipole antenna; dual-polarized; low-profile; wideband artificial magnetic conductor



Citation: Feng, H.; Li, M.; Zhang, Z.; Fu, J.; Zhang, Q.; Zhao, Y. Low-Profile Broadband Dual-Polarized Dipole Antenna for Base Station Applications. *Sensors* **2023**, *23*, 5647. <https://doi.org/10.3390/s23125647>

Academic Editor: Guy A. E. Vandebosch

Received: 8 May 2023

Revised: 12 June 2023

Accepted: 14 June 2023

Published: 16 June 2023



Copyright: © 2023 by the authors. Licensee MDPI, Basel, Switzerland. This article is an open access article distributed under the terms and conditions of the Creative Commons Attribution (CC BY) license (<https://creativecommons.org/licenses/by/4.0/>).

1. Introduction

As wireless communication networks expand, base station antennas are critical components in these systems. However, they face challenges, such as large physical dimensions and limited bandwidth [1]. Dual-polarized antennas have received great attention due to their advantages in polarization diversity and high isolation, which can increase channel capacity. Practically, various antenna designs can achieve dual polarization. Common elements can include patch antennas [2,3], slot antennas [4], or dipole antennas [5–16]. However, they may suffer from either a limited bandwidth [2–4] or a high profile [5–7]. Achieving miniaturization and widening the bandwidth have emerged as the foremost challenges in developing dual-polarized antennas.

Dual-polarized planar dipole antennas have attracted considerable attention because of their wide bandwidth and pattern stability. Low-profile designs can be achieved using bowtie-shaped crossed-dipole antennas and Huygens dipole antennas, with profiles of $0.088\lambda_0$ [8] and $0.0483\lambda_0$ [9], respectively (where λ_0 represents the wavelength in free space at the center frequency). However, they can provide narrow -10 -dB impedance bandwidths of only 15.6% [8] and 0.462% [9]. To enhance the antenna bandwidth, parasitic elements are used in antenna design. The common parasitic element can be L-shaped metal strips [10] or quadrangular loops [11,12]. They act as additional resonating elements, creating a coupling effect [10] or adding a new resonant mode [11,12]. As a result, the overall bandwidth significantly improved. The parasitic U-shaped grooves are also utilized to broaden the bandwidth [13,14]. Grooves can modify the current distribution on the main radiating element and, thus, improve the antenna impedance. However, the profile of those dipole designs is around a quarter wavelength due to the conventional conductor reflector. The profile is required to eliminate the effect of reflected electromagnetic waves

from the reflector. This bulkiness increases the cost and may not be suitable for size-constrained applications.

Frequency Selective Surfaces have recently obtained much attention due to their unique properties in favor of antenna performance. A frequency selective surface (FSS) is a periodic structure, typically a thin sheet or a grid, that has unique transmission and reflection properties for different electromagnetic frequencies. These surfaces are designed to either pass or block specific frequency ranges when subject to electromagnetic radiation. The FSS is useful in antenna design, such as reducing decoupling [15,16] and increasing gain [17,18]. FSSs are usually located on the top of the antenna radiation aperture to realize some specific functions. This method is effective and straightforward. However, it will introduce extra antenna length, which may limit its practical applications.

As a kind of FSS, the artificial magnetic conductor (AMC) is useful in addressing antenna size problems. It can replace a traditional metal conductor as a new reflector type for base station antennas. They exhibit properties of magnetic conductors with a zero-degree phase shift upon reflection. The in-phase reflection avoids the 180-degree phase change of the electromagnetic wave when it is reflected from the metal plate, thus, eliminating the need to set the reflector back at $1/4 \lambda_0$ from the radiator. As a result, this characteristic enables them to reduce the antenna profile, leading to compact and low-profile antenna designs. In [8], using a circle-typed AMC, the profile of a dipole antenna is effectively reduced to $0.088\lambda_0$. However, its -10 -dB impedance bandwidth is only 15.6% (2.36–2.76 GHz). In [19], using mushroom-type AMC, a patch antenna has an impedance bandwidth of 33% (24.05–33.52 GHz) with a profile of $0.053\lambda_0$.

Air gap technology has obtained much attention due to its ease of fabrication and high performance in antenna applications [20]. Adding an air gap in AMC can expand the in-phase bandwidth of AMC. In [21,22], dual-polarized dipole antennas using AMC reflectors have heights of $0.13\lambda_0$ and $0.15\lambda_0$. These antennas have a wide AMC bandwidth of more than 40%. However, both designs suffer from strong surface waves, leading to decreased antenna gain [21] or high cross-polarization at big angles [22]. Therefore, designing a wideband AMC that can suppress surface waves is highly desired.

In this paper, a low-profile broadband dual-polarized dipole antenna using a novel AMC reflector is investigated. Using the Brillouin dispersion diagram, the AMC is designed to suppress the surface-wave effect and decrease the antenna height. As a result, the proposed antenna has a high efficiency and low antenna profile. The fork-shaped lines feed the antenna without a direct connection, giving a broad impedance bandwidth. The parasitic strips reduce cross-polarization. The evolution of the proposed AMC and dipole antenna is analyzed using equivalent circuits and Smith charts. A prototype that operates in 2G/3G/LTE base station applications was designed and fabricated. The reflection coefficient, radiation pattern, antenna gain, and antenna efficiency are measured. Reasonable agreement between the measured and simulated results is obtained.

2. Antenna Design and Configuration

Figure 1 shows the configuration of the wideband dual-polarized antenna. With reference to Figure 1a,b, this antenna comprises crossed-dipoles, double-layer AMC, fork-shaped feeding structures, and parasitic strips. Two crossed dipoles are positioned perpendicularly with slant angles of $\varphi = \pm 45^\circ$ and are represented as dipoles 1 and 2. Figure 1c shows the exploded view of the proposed antenna. It can be seen from the figure that the feeding lines and crossed dipoles are printed on Layers 1 and 2 of Substrate 1 (Sub. 1), respectively. Figure 1d zooms in view of the arms of dipoles and feeding structures. As can be seen from the figure, each arm of the dipole is a hexagonal ring with a width of $w_1 = 3.6$ mm and four mirror-symmetrical etched slots. It should be mentioned that one of the dipole arms is soldered directly to the feeding structures, while the other arm is fed via space coupling. This method is designed to obtain a wide -15 -dB impedance matching bandwidth. The novel AMC consists of two metal layers, one substrate, and air layers. Periodic patches are its first metal layer printed on Layer 3 of Sub. 2, with the interval gap of $g = 2$ mm and

patch width of $w = 13$ mm. The second metal layer is aluminum ground. Sub. 1 and Sub. 2 are FR4 substrates ($\epsilon_r = 4.4$, $\tan\delta = 0.02$). Crossed dipoles are placed at a height of 5.5 mm from the AMC surface. Plastic pins are used to locate layers precisely. Figure 2 shows the different layers of the dual-polarized antenna. With reference to the figure, our parasitic strips are printed on Layer 2 of Substrate 1 to reduce cross-polarization.

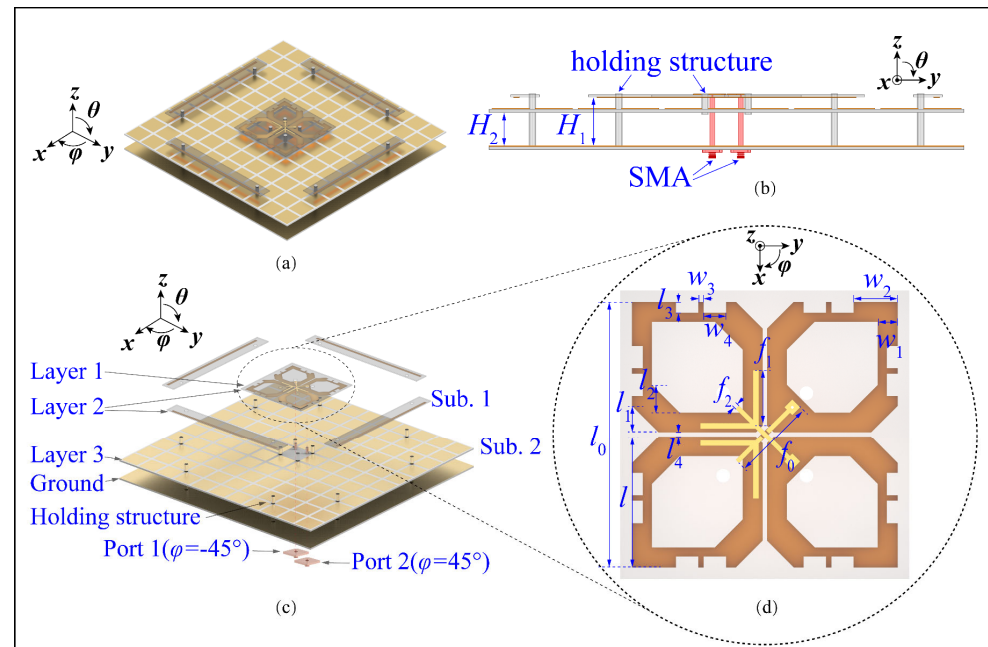


Figure 1. Configuration of the dual-polarized antenna. (a) Perspective view, (b) side view, (c) exploded view, and (d) zoomed view of crossed-dipole antenna. $H_1 = 17.5$ mm, $H_2 = 12$ mm, $w_1 = 3.6$ mm, $w_2 = 7.3$ mm, $w_3 = 1.65$ mm, $w_4 = 4$ mm, $l = 23.5$ mm, $l_0 = 52$ mm, $l_1 = 4.8$ mm, $l_2 = 5$ mm, $l_3 = 2$ mm, $l_4 = 0.8$ mm, $f_0 = 14$ mm, $f_1 = 10.5$ mm, $f_2 = 0.83$ mm.

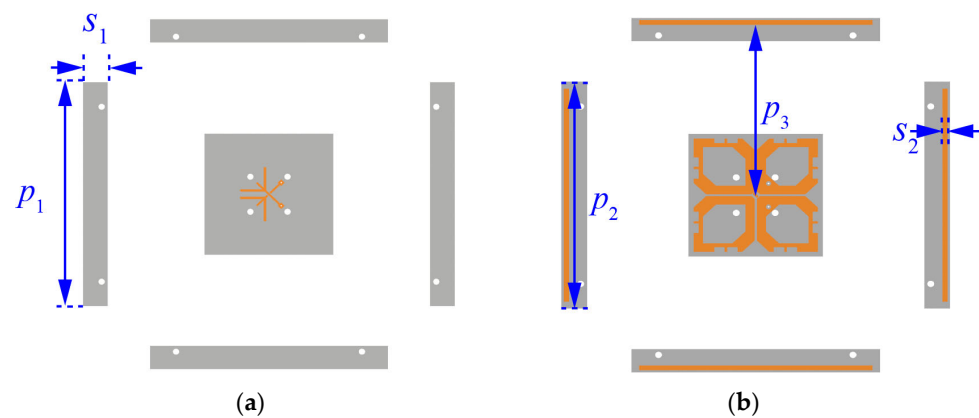


Figure 2. Cont.

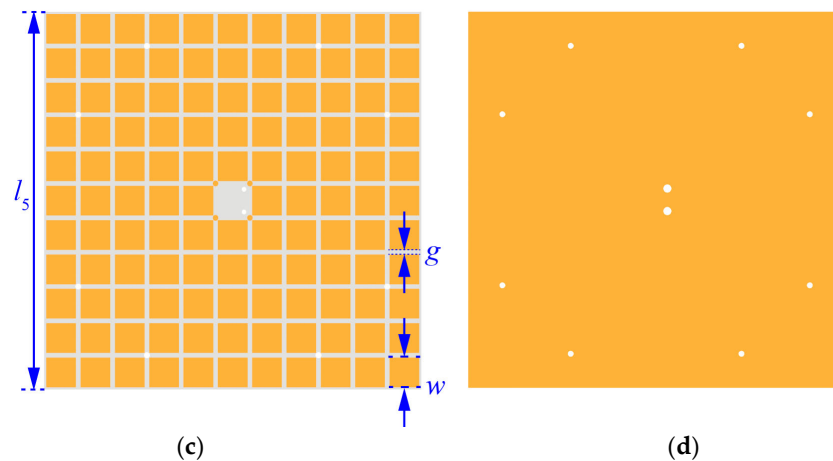


Figure 2. Different layers of the dual-polarized antenna: (a) Substrate 1 Layer 1, (b) Substrate 1 Layer 2, (c) Substrate 2 Layer 3, and (d) aluminum ground. $l_5 = 65$ mm, $w = 13$ mm, $g = 2$ mm, $S_1 = 10$ mm, $S_2 = 2$ mm, $P_1 = 96$ mm, $P_2 = 90$ mm, $P_3 = 72$ mm.

3. Analysis and Discussion

3.1. In-Phase Reflection Bandwidth of the AMC Unit

Figure 3 shows the configurations and reflection coefficients of different AMC units. The proposed AMC is a patch-type with a patch length and width of $w = 13$ mm, a substrate-layer height of $h_d = 1.2$ mm ($0.0088\lambda_0$), and an air-layer height of $h_a = 12$ mm ($0.088\lambda_0$). AMC₁ and AMC₂, which are conventional AMCs with the same patch size and gap width but different substrate-layer heights ($h_{d1} = 1.2$ mm, $h_{d2} = 9.5$ mm), were simulated for comparison. Generally, the in-phase reflection bandwidth is the frequency range in which the reflection phase is between $-\pi/2$ and $\pi/2$. With reference to the figure, the in-phase reflection bandwidths are 9.8%, 39.4%, and 54.7% for AMC₁ (4.57–5.04 GHz), AMC₂ (1.67–2.49 GHz), and the proposed AMC (1.54–2.70 GHz), respectively. Compared with the proposed AMC, AMC₁ lacks the air layer, giving a zero-phase reflection frequency of 4.82 GHz that is out of the operating bandwidth of 2G/3G/LTE. It is worth mentioning that AMC₂ has almost the same zero-phase reflection frequency, however, it has a narrower in-phase bandwidth and a worse reflection coefficient than the proposed AMC. Therefore, our AMC is a good alternative to the metal ground due to its wideband.

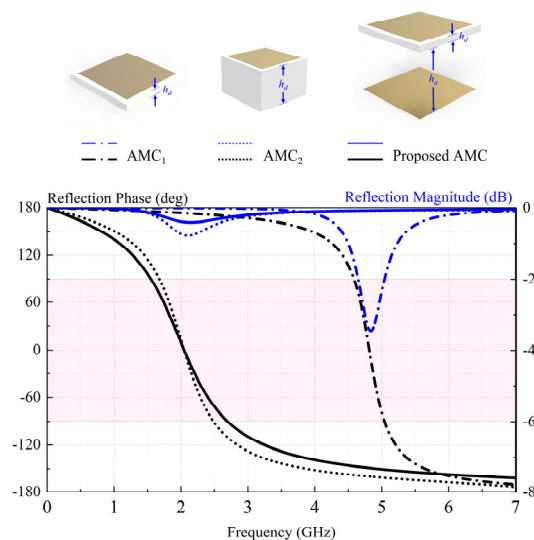


Figure 3. Reflection coefficients and configurations of different AMC units. The pink area is the in-phase reflection bandwidth.

The proposed AMC unit can be equivalent to an LC parallel resonant circuit using the equivalent circuit analysis method (ECM) [23,24], as illustrated in Figure 4. Periodical patches provide the grid inductance L_p . Another inductance L_d is created by the total substrate, including the air and the dielectric. Gaps between adjacent patches form a grid capacitance C_p . As a result, the resonant frequency and bandwidth of the proposed AMC can be represented by Equations (1) and (2), which show the relationship between parameters on the resonant frequency and bandwidth coefficient.

$$f = \frac{1}{2\pi\sqrt{(L_p + L_d)C_p}}, \quad (1)$$

$$BW = \frac{\pi}{8\eta_0} \sqrt{\frac{L_p + L_d}{C_p}} \times \left(\frac{L_d}{L_p + L_d}\right)^2, \quad (2)$$

where $\eta_0 = \sqrt{\mu_0/\epsilon_0}$ is the wave impedance in free space. Compared with AMC₁ and AMC₂, the proposed AMC has higher profiles and, thus, a larger dielectric inductance L_d . Since the derivative of Equation (2) with respect to L_d is positive, the bandwidth is positively related to the dielectric inductance L_d . Therefore, AMC₂ and the proposed AMC have a wider bandwidth. In addition, the dielectric substrate of AMC₂ is thicker, which increases dielectric losses and manufacturing costs. The proposed AMC has the widest bandwidth. The surface impedance of AMC can be represented by:

$$\eta_s(f) = j2\pi f L_d \frac{1 - (2\pi f)^2 L_p C_p}{1 - (2\pi f)^2 (L_p + L_d) C_p}. \quad (3)$$

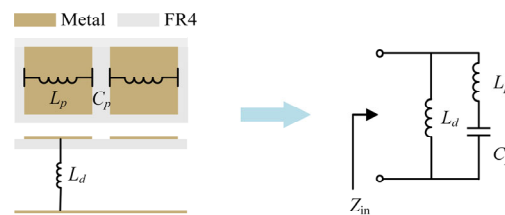


Figure 4. Equivalent circuit model of the proposed AMC unit.

At the parallel resonant frequency (using Equation (1)), the denominator of Equation (3) is equal to zero, and thus, the surface impedance η_s tends to infinity. The reflection coefficient of AMC can be calculated by $\Gamma = (\eta_s - \eta_0)/(\eta_s + \eta_0)$, where η_0 equals the impedance of air. Therefore, the reflection coefficient equals one, and the reflection phase is zero. AMC achieves the in-phase reflection at the resonant frequency.

3.2. Brillouin Dispersion Diagram of the AMC Unit

Generally, a surface wave will be excited when electromagnetic waves reflect from the ground, deteriorating antenna performance. Figure 5 shows the dispersion curves of the proposed AMC unit. With reference to the figure, the electromagnetic wave under 2.65 GHz served as a slow wave and bounded in the AMC surface. However, as the frequency increases beyond 2.65 GHz, the electromagnetic wave gradually becomes a fast wave and leaks into free space. Consequently, antennas loading the proposed AMC and the conventional metal ground have nearly the same realized gain before 2.65 GHz, as shown in Figure 6a. Figure 6b shows the simulated S-parameters of the antenna. It can be seen from the figure that both the reflection coefficient and isolation are improved by using the AMC. It should be mentioned that the proposed antenna can effectively decrease the antenna profile from $0.25\lambda_0$ to 0.13λ .

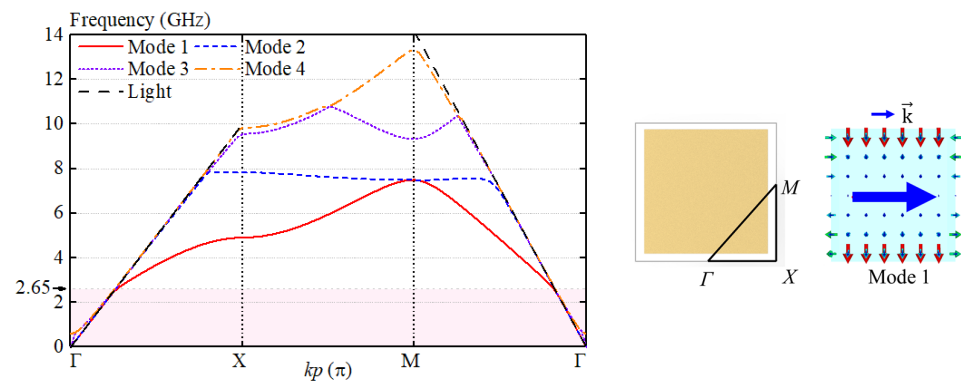


Figure 5. The dispersion curves of the proposed AMC unit. The illustrations are the electric field distributions. The blue arrow indicates the direction of propagating wave.

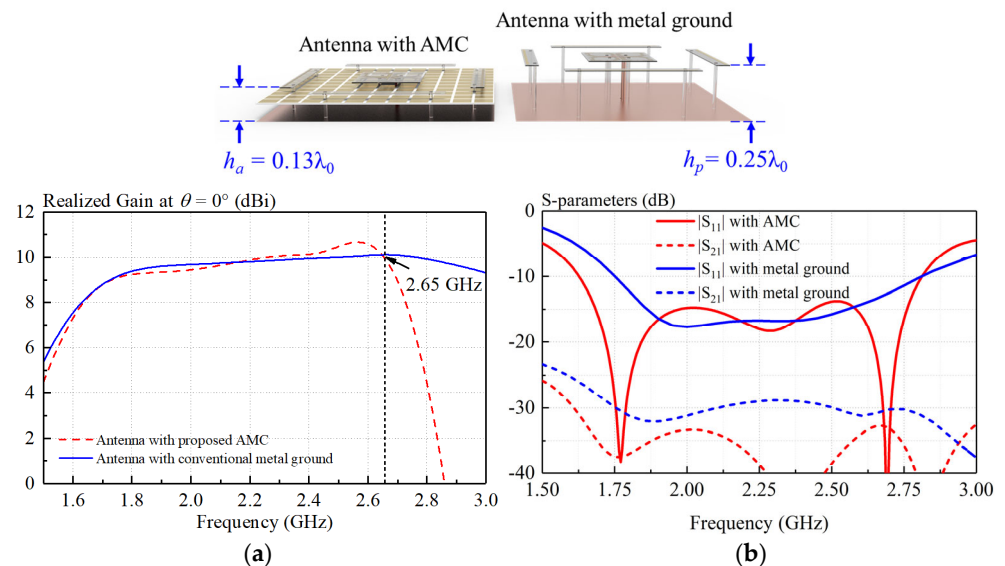


Figure 6. Comparison between crossed-dipole antenna with AMC and that with conventional metal ground. (a) Simulated realized gain, (b) simulated S-parameters.

3.3. Evolution of the Antenna

Figure 7 shows the design evolution of the crossed dipole and compares the simulated reflected coefficient of Dipole I, II, and III. Figure 8 provides electrical current distributions of different dipoles at their respective resonant frequencies. With reference to Figure 7, Dipole I is a conventional rectangular dipole with only one resonant mode (seen in Figure 8a), having a -10 -dB impedance bandwidth of 29.9% (1.88–2.54 GHz). Dipole II is obtained by cutting the arm corners and centers of Dipole I, which introduces a new resonant mode f_{21} in the lower-frequency band. Therefore, Dipole II has a wide -10 -dB impedance bandwidth of 41.7% (1.67–2.55 GHz). This can be well-demonstrated by Figure 8b. The surface current distribution at f_{11} and f_{23} is the same.

Dipole III is obtained by adding rectangular slots on Dipole II. The introduced rectangular slots effectively make two different resonant modes close (seen in Figure 8c), resulting in a wide-impedance passband of 55.4% (1.58–2.79 GHz).

Figure 9 also shows the Smith charts of antennas with different dipoles. The Smith chart of Dipole I has no resonant loop, while the Smith charts of Dipole II and Dipole III have 1 and 2 resonant loops, respectively. Dipole III achieves a wider impedance bandwidth by cutting arm corners and centers and adding rectangular slots.

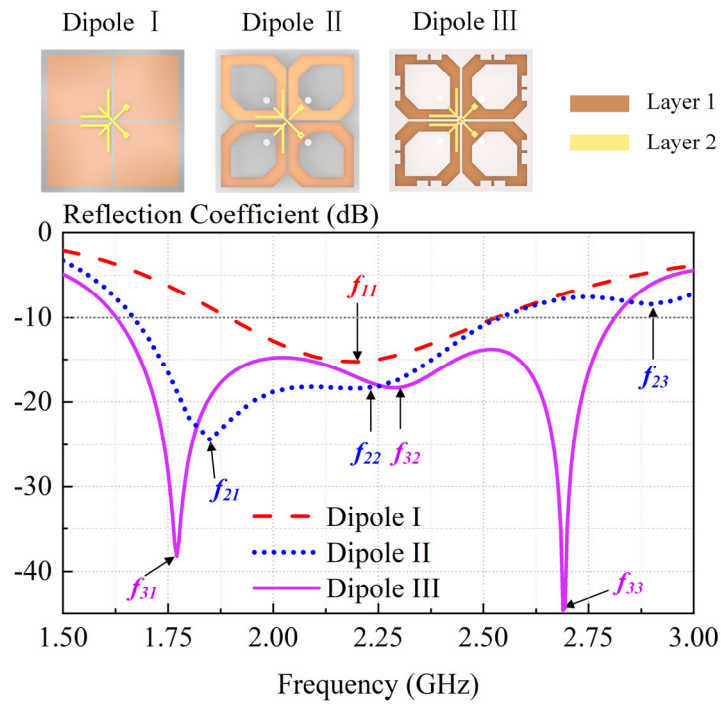


Figure 7. Schematic diagrams and simulated reflection coefficients of Dipole I, Dipole II, and Dipole III. Dipole I (a conventional crossed-dipole antenna), Dipole II (Dipole I with corners and centers cut), and Dipole III (crossed dipole in proposed antenna).

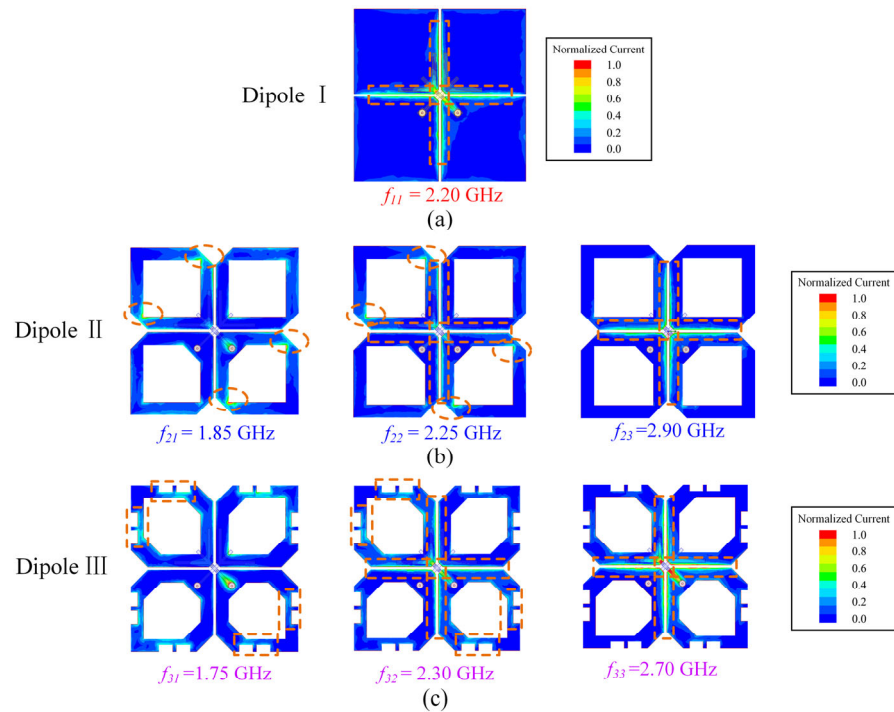


Figure 8. Electrical current distributions of (a) Dipole I, (b) Dipole II, and (c) Dipole III.

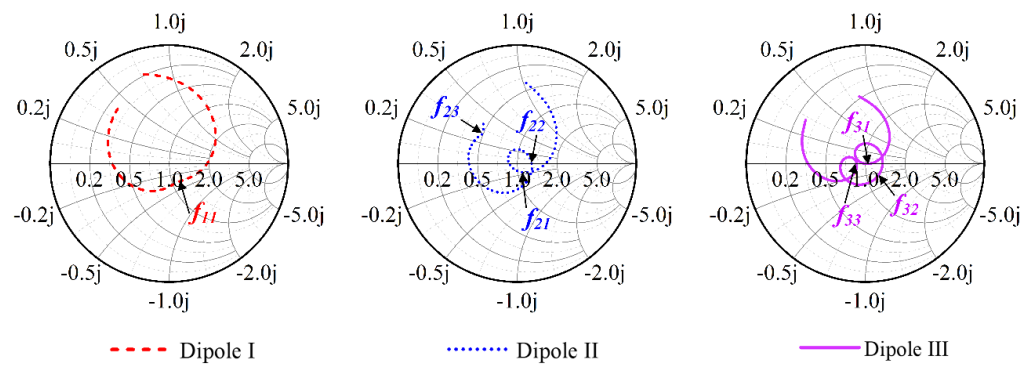


Figure 9. Smith charts of antennas of Dipole I, Dipole II, and Dipole III.

The equivalent circuit model of Dipole III is shown in Figure 10a. According to previous studies [25,26], the feeding structure is modeled as a parallel LC resonator circuit (L_f and C_f) and a π -shaped network (C_{g1} , C_{g11} , and C_{g12}). Dipole III is obtained by cutting corners and opening rectangular slots in Dipole I. Dipole I can be expressed as a parallel RLC resonator circuit (R_{d1} , L_{d1} , and C_{d1}). The corners and rectangular slots can be expressed as a parallel RLC resonator circuit (R_{s1} , L_{s1} , and C_{s1}). When one loop dipole is excited, the other acts as a coupled loop resonator. Consequently, they are configured in parallel within the circuit. The adjacent gaps between two dipoles are modeled as a π -shaped network (C_{g2} , C_{g21} , and C_{g22}).

By utilizing the proposed equivalent circuit and circuit analysis software, we can expedite the design process of the proposed antenna, particularly when attempting to bring two resonant modes into proximity. The values of circuit parameters can be obtained by using a curve-fitting method. The extracted results are $L_f = 1.73$ nH, $C_f = 0.10$ pF, $C_{g1} = 3.48$ pF, $C_{g11} = 0.43$ pF, $C_{g12} = 4.17$ pF, $R_{d1} = 99.9$ Ω , $L_{d1} = 1.07$ nH, $C_{d1} = 0.36$ pF, $R_{s1} = 5.02$ Ω , $L_{s1} = 1.07$ nH, $C_{s1} = 2.23$ pF, $C_{g2} = 2.45$ pF, $C_{g21} = 0.43$ pF, $C_{g22} = 4.17$ pF, $R_{d2} = 5.24$ Ω , $L_{d2} = 0.35$ nH, $C_{d2} = 3.18$ pF, $R_{s2} = 5.24$ Ω , $L_{s2} = 0.35$ nH, $C_{s2} = 2.93$ pF. Figure 10b shows the reflection coefficient derived from the equivalent circuit model and that from the HFSS.

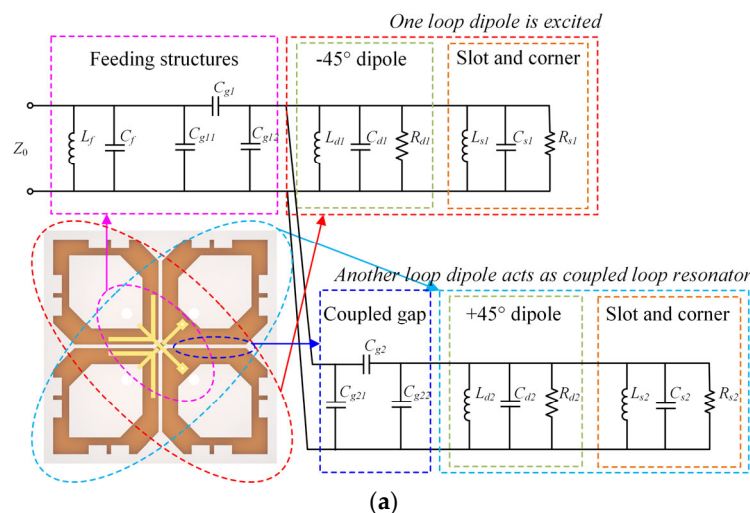


Figure 10. Cont.

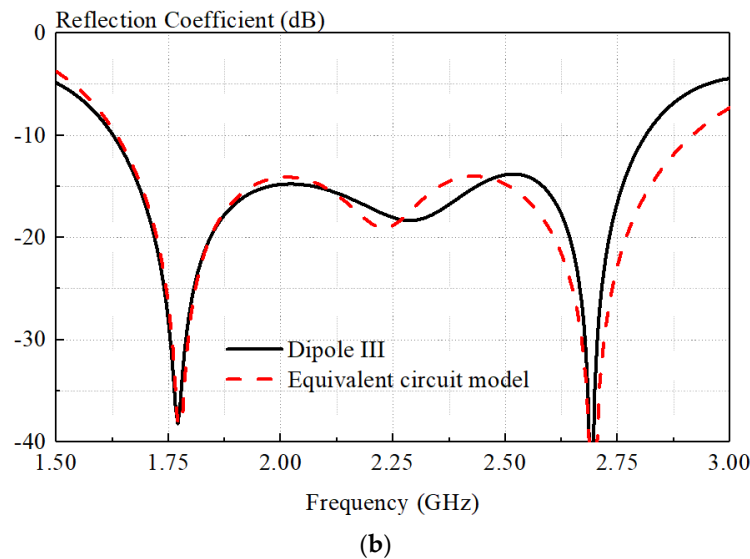


Figure 10. (a) Equivalent circuit model of Dipole III. (b) Reflection coefficient of Dipole III obtained from the equivalent circuit model and that from the HFSS.

AMC is employed to replace the traditional metal ground, thereby increasing the antenna gain and maintaining a low profile. Therefore, it becomes crucial to select an appropriate quantity of AMC units. This strategic selection aims to ensure that the antenna exhibits a broad, high-gain bandwidth, adequately covering the frequency ranges of 2G (1.71–1.92 GHz), 3G (1.88–2.17 GHz), and LTE (2.3–2.4 GHz and 2.5–2.69 GHz) networks. Figure 11 shows the simulated realized gains of the proposed antenna with different numbers ($m \times m$) of AMC units. With reference to Figure 11, when the number of elements is 11×11 , the proposed antenna has the highest average gain across the bandwidth of 1.71–2.69 GHz. Therefore, the number 11×11 is chosen for AMC design.

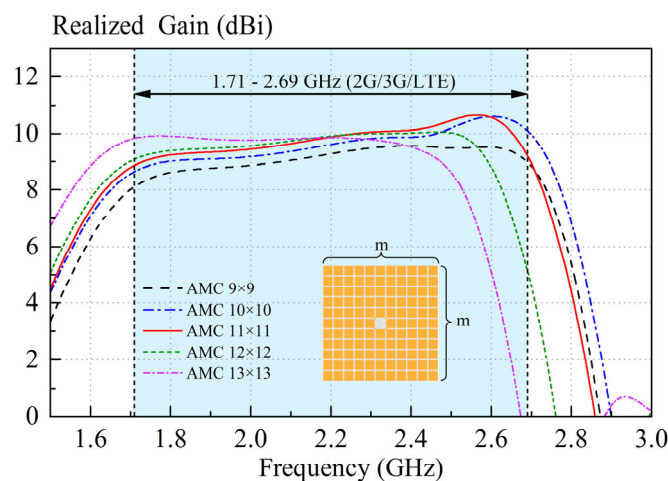


Figure 11. Simulated realized gain for proposed antenna under different numbers ($m \times m$) of AMC units. The blue region is the commercial bands for 2G, 3G, and LTE.

Figure 12 shows the comparison of simulated radiation patterns between the crossed-dipole antenna with/without four parasitic strips. With reference to the figure, significant improvements in both E - and H -plane radiation patterns can be obtained by the loading strips. It is worth mentioning that, using this method, the cross-polar fields in the two principal cutting planes decrease by more than 12 dB.

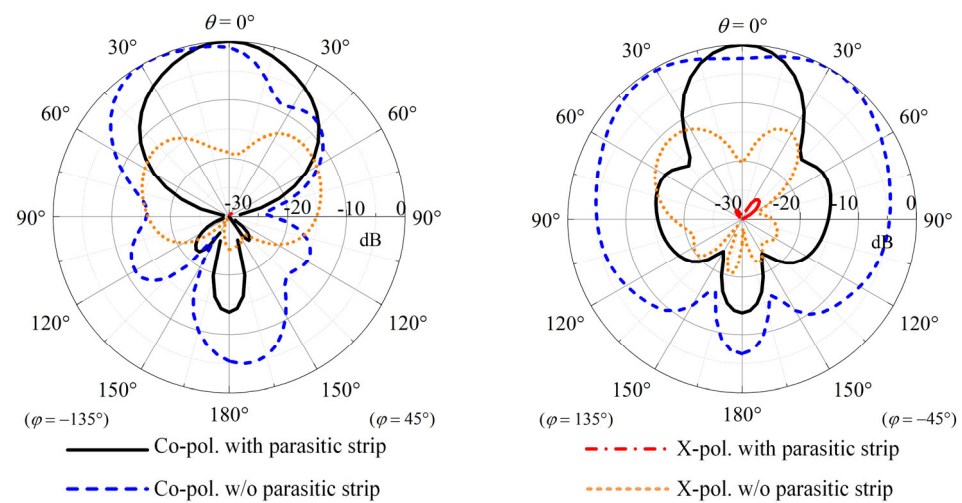


Figure 12. Comparison of simulated radiation patterns between the antennas with/without parasitic strips.

4. Results

To verify the idea, a prototype of the proposed antenna was fabricated, as shown in Figure 13. Figure 14 shows the measured and simulated S-parameter of our antenna. With reference to Figure 14a, the measured and simulated -10 -dB impedance bandwidths ($|S_{11}| \leq -10$ dB) are 54.05% (1.62–2.82 GHz) and 55.37% (1.58–2.79 GHz), respectively. As shown in Figure 14b, the isolations in both the simulation and measurement are almost greater than 30 dB across the impedance-matching passband. As can be observed from Figure 14, reasonable agreement between the measured and simulated results is observed. Acceptable errors are caused by slight deformation due to uneven structural support. The designed antenna exhibits good broadband characteristics and high isolation.

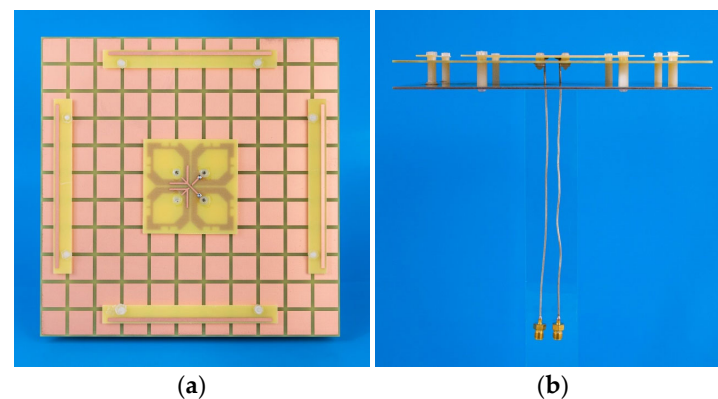


Figure 13. Photograph of proposed antenna. (a) Top view, (b) side view.

Figure 15a presents simulated and measured realized gains of the proposed antenna at $\theta = 0^\circ$. With reference to the figure, reasonable agreement can be found between the simulated and measured results. The ripple in measurement is less than 1 dB caused by experimental imperfections. The measured gain varies between 8.3 and 10.8 dB over the frequency range (1.62–2.82 GHz) shown in Figure 15a. Figure 15b shows the measured antenna efficiency of the low-profile crossed-dipole antenna. As can be observed from Figure 15b, the measured antenna efficiency is higher than 90% across the entire operating band.

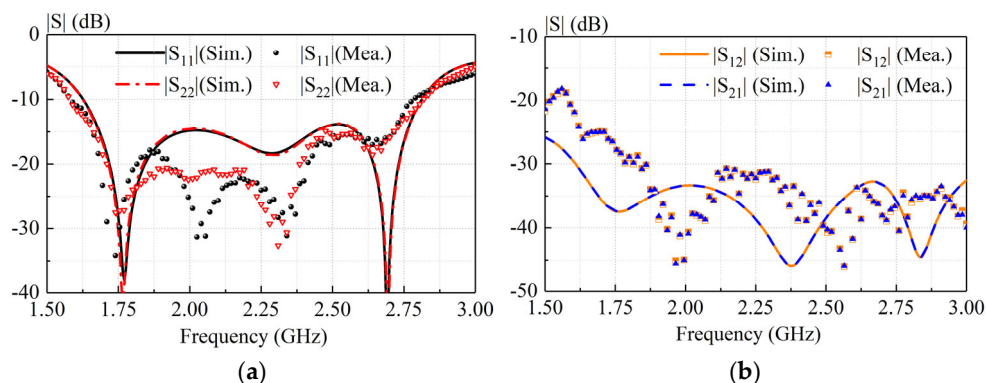


Figure 14. Measured and simulated S-parameters of proposed antenna.

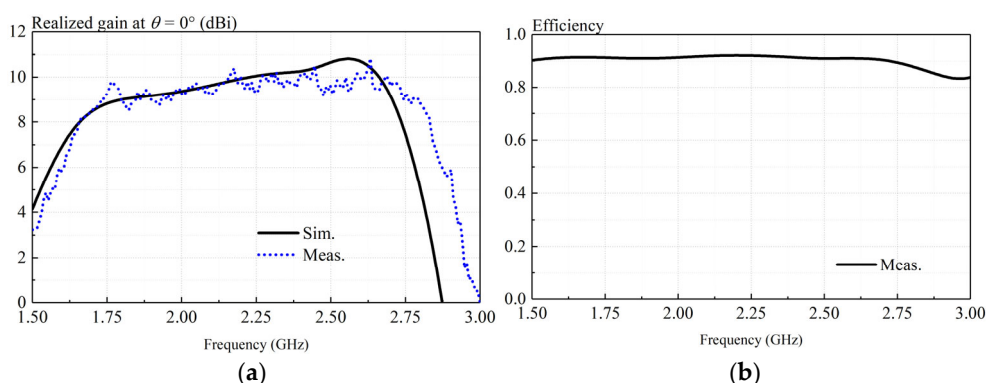


Figure 15. Measurements and simulations of proposed antenna. (a) Realized gain; (b) antenna efficiency.

Figure 16 shows the measured and simulated normalized radiation patterns in two principal cutting planes. Reasonable agreement can be found between simulations and measurements. As shown in the figure, stable radiation patterns can be found at three different frequencies. The simulated cross-polar field is almost lower than -30 dB. It can be observed from the figure that the co-polar field is 10 dB higher than the cross-polar field over a wide range of angles ($-60^\circ < \theta < 60^\circ$) in the measurements. Results of Port 1 are only shown due to the geometric symmetry of our crossed-dipole antenna.

Table 1 compares our antenna with the reported crossed-dipole antennas. With reference to the table, the antennas in [8,9] have an extremely low antenna height but a narrow bandwidth and low gain. The designs in references [11–14] have a higher profile. The antennas in references [14,21] have similar profiles, but their antenna gains are lower than the proposed antenna. Our wideband dual-polarized antenna has the highest antenna efficiency due to the proposed AMC. Compared with listed base-station antennas, the proposed antenna outperforms in overall performance. It is a good candidate for base-station applications.

Table 1. Comparison of crossed-dipole antennas.

Ref.	−10-dB Impedance Bandwidth	Gain (dBi)	Isolation (dB)	Antenna Efficiency	Profile (λ_0)
[8]	15.6% (2.36–2.76 GHz)	4.6–7.2	>22	65.0%	0.09
[9]	0.46% (1.48–1.55 GHz)	<2.2	>26	61.3%	0.05
[11]	52.2% (1.70–2.90 GHz) (VSWR < 1.5)	8.2–9.4	>26	N.A.	0.26
[12]	48.7% (1.66–2.73 GHz)	7.8–8.5	>34	85.0%	0.23

Table 1. Cont.

Ref.	−10-dB Impedance Bandwidth	Gain (dBi)	Isolation (dB)	Antenna Efficiency	Profile (λ_0)
[13]	65.3% (1.67–3.29 GHz)	7.8–8.8	>32	90%	0.26
[14]	74.9% (1.31–2.88 GHz)	7.8~9.1	>30	N.A.	0.35
[21]	56.3% (1.67–2.98 GHz)	6.7–7.6	>25	80%	0.13
[22]	49.4% (1.69–2.80 GHz)	6.8–9.8	>27	86%	0.15
This work	55.4% (1.58–2.79 GHz)	8.3–10.8	>30	90%	0.13

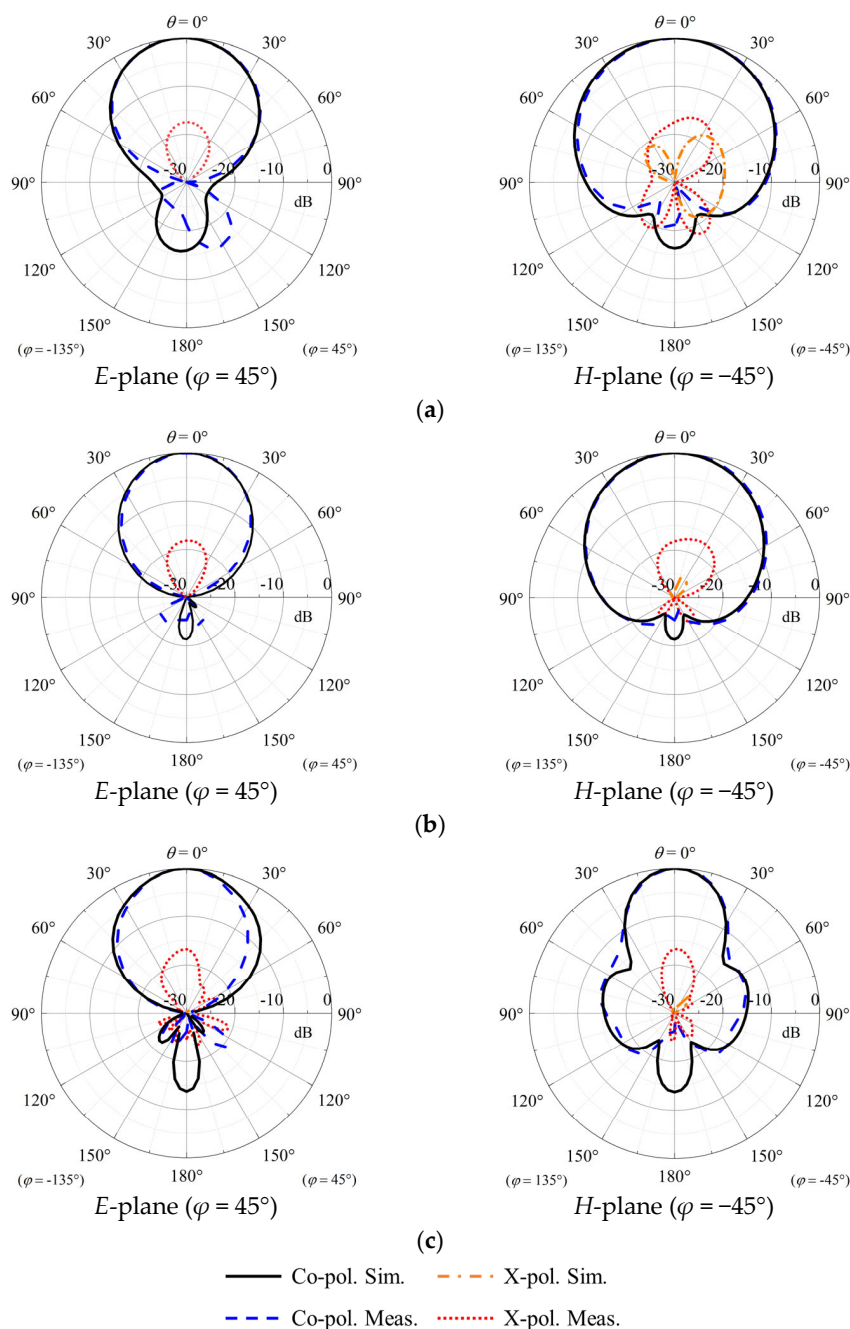


Figure 16. Measured and simulated radiation patterns of proposed antenna Port 1. (a) 1.6 GHz, (b) 2.1 GHz, and (c) 2.6 GHz. Results of Port 1 are only shown due to the geometric symmetry of our crossed-dipole antenna.

5. Conclusions

A wideband low-profile crossed-dipole antenna with a novel AMC has been investigated. By introducing the AMC as antenna ground, the profile can be effectively decreased to $0.12\lambda_0$. In addition, four parasitic metal strips have been introduced to reduce the cross-polar field and, thus, increase the antenna gain in its high-frequency impedance passband. To verify the idea, a prototype has been simulated, fabricated, and measured. A measured overlapping bandwidth of 55.4% (1.58–2.79 GHz) has been obtained. Its maximum measured realized gain is 10.8 dB at 2.6 GHz. Additionally, a stable gain and radiation pattern have been observed. The prototype has a measured isolation of ~ 30 dB. It should be mentioned that its cross-polarization level is more than -10 dB over a wide range of angles ($-60^\circ < \theta < 60^\circ$). Finally, these advantages enable the proposed antenna to be potentially applied to the integrated design of 2G/3G/LTE base station antennas.

Author Contributions: Conceptualization, methodology, Z.Z. and H.F.; validation, M.L.; formal analysis, H.F. and Q.Z.; writing—review and editing, Y.Z.; project administration, J.F. All authors have read and agreed to the published version of the manuscript.

Funding: This research was funded by the National Natural Science Foundation of China under Grant 62171165.

Institutional Review Board Statement: Not applicable.

Informed Consent Statement: Not applicable.

Data Availability Statement: Not applicable.

Acknowledgments: The useful comments by the anonymous reviewers are gratefully appreciated.

Conflicts of Interest: The authors declare no conflict of interest. The funders had no role in the design of this study, including the collection, analyses, or interpretations of data, in the writing of the manuscript, or in the decision to publish the results.

References

1. Huang, C.; Zappone, A.; Alexandropoulos, G.C.; Debbah, M.; Yuen, C. Reconfigurable intelligent surfaces for energy efficiency in wireless communication. *IEEE Trans. Wirel. Commun.* **2019**, *18*, 4157–4170. [[CrossRef](#)]
2. Li, Q.L.; Cheung, S.W.; Zhou, C.F. A low-profile dual-polarized patch antenna with stable radiation pattern using ground-slot groups and metallic ground wall. *IEEE Trans. Antennas Propag.* **2017**, *65*, 5061–5068. [[CrossRef](#)]
3. Zhang, X.; Xue, D.; Ye, L.; Pan, Y.; Zhang, Y. Compact dual-band dual-polarized interleaved two-beam array with stable radiation pattern based on filtering elements. *IEEE Trans. Antennas Propag.* **2017**, *65*, 4566–4575. [[CrossRef](#)]
4. Liu, Y.; Li, X.; Yang, L.; Liu, Y. A dual-polarized dual-band antenna with omni-directional radiation patterns. *IEEE Trans. Antennas Propag.* **2017**, *65*, 4259–4262. [[CrossRef](#)]
5. Dai, X.W.; Ding, C.; Zhu, F.; Liu, L.; Luo, G.Q. Broadband dual-polarized element with rotated sleeve arms for compact dual-band antenna. *IEEE Antennas Wirel. Propag. Lett.* **2021**, *20*, 2519–2523. [[CrossRef](#)]
6. Wu, R.; Chu, Q.X. A wideband dual-polarized antenna for LTE700/GSM850/GSM900 applications. *IEEE Antennas Wirel. Propag. Lett.* **2017**, *16*, 2098–2101. [[CrossRef](#)]
7. Huang, H.; Liu, Y.; Gong, S.X. A dual-broadband, dual-polarized base station antenna for 2G/3G/4G applications. *IEEE Antennas Wirel. Propag. Lett.* **2017**, *16*, 1111–1114. [[CrossRef](#)]
8. Zhai, H.; Zhang, K.; Yang, S.; Feng, D. A low-profile dual-band dual-polarized antenna with an AMC surface for WLAN applications. *IEEE Antennas Wirel. Propag. Lett.* **2017**, *16*, 2692–2695. [[CrossRef](#)]
9. Tang, M.C.; Wu, Z.T.; Shi, T.; Zeng, H.; Lin, W.; Ziolkowski, R.W. Dual-linearly polarized, electrically small, low-profile, broadside radiating, Huygens dipole antenna. *IEEE Trans. Antennas Propag.* **2018**, *66*, 3877–3885. [[CrossRef](#)]
10. Yu, W.; Lin, H.; Liao, B.; Duan, W. A compact dual-polarized low-pass filtering antenna with wideband out-of-band rejection. *IEEE Antennas Wirel. Propag. Lett.* **2021**, *20*, 2329–2333. [[CrossRef](#)]
11. Wen, D.L.; Zheng, D.Z.; Chu, Q.X. A wideband differentially fed dual-polarized antenna with stable radiation pattern for base stations. *IEEE Trans. Antennas Propag.* **2017**, *65*, 2248–2255. [[CrossRef](#)]
12. Ding, C.F.; Zhang, X.Y.; Zhang, Y.; Pan, Y.M.; Xue, Q. Compact broadband dual-polarized filtering dipole antenna with high selectivity for base-station applications. *IEEE Trans. Antennas Propag.* **2018**, *66*, 5747–5756. [[CrossRef](#)]
13. Ding, C.F.; Zhang, X.Y.; Yu, M. Simple dual-polarized filtering antenna with enhanced bandwidth for base station applications. *IEEE Trans. Antennas Propag.* **2020**, *68*, 4354–4361. [[CrossRef](#)]

14. Cui, Y.; Wu, L.; Li, R. Bandwidth enhancement of a broadband dual-polarized antenna for 2G/3G/4G and IMT base stations. *IEEE Trans. Antennas Propag.* **2018**, *66*, 7368–7373. [[CrossRef](#)]
15. He, D.L.; Chen, Y.K.; Yang, S.W. A low-profile triple-band shared-aperture antenna array for 5G base station applications. *IEEE Trans. Antennas Propag.* **2022**, *70*, 2732–2739. [[CrossRef](#)]
16. He, D.L.; Yu, Q.; Chen, Y.K.; Yang, S.W. Dual-band shared-aperture base station antenna array with electromagnetic transparent antenna elements. *IEEE Trans. Antennas Propag.* **2021**, *69*, 5596–5606. [[CrossRef](#)]
17. Al-Gburi, A.J.A.; Ibrahim, I.B.; Zeain, M.Y.; Zakaria, Z. Compact size and high gain of CPW-fed UWB strawberry artistic shaped printed monopole antennas using FSS single layer reflector. *IEEE Access* **2020**, *8*, 92697–92707. [[CrossRef](#)]
18. Sheng, X.J.; Lu, X.L.; Liu, N.; Liu, Y.H. Design of broadband high-gain Fabry-Perot antenna using frequency-selective surface. *Sensors* **2022**, *22*, 15. [[CrossRef](#)]
19. Cheng, H.; Xiao, G.B.; Wang, X.C. A low-profile wideband patch antenna with modified parasitic mushroom structures on nonperiodic AMC. *IEEE Antennas Wirel. Propag.* **2023**, *22*, 719–723. [[CrossRef](#)]
20. Keriee, H.H.; Rahim, M.; Nayyef, N.A.; Zakaria, Z.; Al-Gburi, A.J.; Al-Dhief, F.T.; Jawad, M.M. High gain antenna at 915 MHz for off grid wireless networks. *Bull. Electr. Eng. Inform.* **2020**, *9*, 2449–2454. [[CrossRef](#)]
21. Li, M.; Li, Q.L.; Wang, B.; Zhou, C.F.; Cheung, S.W. A low-profile dual-polarized dipole antenna using wideband AMC reflector. *IEEE Trans. Antennas Propag.* **2018**, *66*, 2610–2615. [[CrossRef](#)]
22. Nasser, S.S.S.; Chen, Z.N. Low-profile broadband dual-polarization double-layer metasurface antenna for 2G/3G/LTE cellular base stations. *IEEE Trans. Antennas Propag.* **2022**, *70*, 75–83. [[CrossRef](#)]
23. Ez-zaki, F.; Belaid, K.A.; Ahmad, S.; Belahrach, H.; Ghammaz, A.; Al-Gburi, A.J.A.; Parchin, N.O. Circuit modelling of broadband antenna using vector fitting and foster form approaches for IoT applications. *Electronics* **2022**, *11*, 16. [[CrossRef](#)]
24. Raad, H.R.; Abbosh, A.I.; Al-Rizzo, H.M.; Rucker, D.G. Flexible and compact AMC based antenna for telemedicine applications. *IEEE Trans. Antennas Propag.* **2013**, *61*, 524–531. [[CrossRef](#)]
25. Liao, Y.; Hubing, T.H.; Su, D.L. Equivalent circuit for dipole antennas in a lossy medium. *IEEE Trans. Antennas Propag.* **2012**, *60*, 3950–3953. [[CrossRef](#)]
26. Chen, Y.Z.; Lin, W.B.; Li, S.; Raza, A. A broadband $+/- 45$ degrees dual-polarized multidipole antenna fed by capacitive coupling. *IEEE Trans. Antennas Propag.* **2018**, *66*, 2644–2649. [[CrossRef](#)]

Disclaimer/Publisher’s Note: The statements, opinions and data contained in all publications are solely those of the individual author(s) and contributor(s) and not of MDPI and/or the editor(s). MDPI and/or the editor(s) disclaim responsibility for any injury to people or property resulting from any ideas, methods, instructions or products referred to in the content.